ELSEVIER

Contents lists available at ScienceDirect

Journal of Membrane Science

journal homepage: www.elsevier.com/locate/memsci



Optimizing hollow fiber membrane oxygenators: A multi-objective approach for improved gas exchange and reduced blood damage

Seyyed Hossein Monsefi Estakhrposhti ^{a,b,*}, Jing Jing Xu ^{a,b}, Margit Gföhler ^a, Michael Harasek ^b

ARTICLE INFO

Keywords: Extracorporeal membrane oxygenation (ECMO) Multi-objective optimization Computational fluid dynamics (CFD) Modified enhanced jaya Pareto front solutions

ABSTRACT

Extracorporeal Membrane Oxygenation provides life-saving support for patients with severe heart and lung dysfunction; however, its implementation is associated with significant complications, including hemolysis and thrombosis. These complications address the need for an improved design of hollow fiber membrane oxygenators. This study presents a multi-objective optimization framework aiming to enhance the gas exchange efficiency while minimizing blood damage. A 2D computational fluid dynamics model, validated with micro-PIV measurements, was developed to simulate 200 fiber configurations defined by three geometric parameters (fiber diameter, distance-to-diameter ratio, and angle) and a flow parameter (blood flow rate). Specific CO2 removal, dead-zone-to-total-area ratio, and hemolysis index were established as objectives, representing gas exchange efficiency, thrombosis potential within the membrane module, and hemolysis, respectively. Objectives were modeled using multivariate polynomial functions with unknown exponents and determined using the modified enhanced Jaya algorithm. Single-objective and multi-objective optimization were performed using Pareto front solutions, followed by weighted sum and goal programming methods to identify optimal arrangements. The findings demonstrated that the maximum obtained specific CO_2 removal, dead-zone-to-total-area ratio, and hemolysis index are 250.3 $\mathrm{mL}_{\mathrm{CO2}}$ min^{-1} m^{-2} , 0.0254 %, and 0.011 \times 10⁻³ %, respectively. Furthermore, this study identifies the distance-to-diameter ratio as the key factor affecting all the objectives. Finally, the calculated optimal configuration from both weighted sum and goal programming methods suggests that the best configuration includes low angle, small diameter, and relatively moderate distance-to-diameter ratio, and high blood flow rate.

1. Introduction

Extracorporeal Membrane Oxygenation (ECMO) is a life-support technique used in critical care to support patients with severe heart and lung dysfunction [1]. The main component of an ECMO circuit is the hollow fiber membrane oxygenator, which facilitates gas exchange by diffusing oxygen into the blood and removing carbon dioxide [2]. During the COVID-19 pandemic, the use of ECMO increased significantly, supporting patients experiencing severe respiratory failure. The increased dependence on ECMO displayed its critical role in managing acute respiratory distress syndrome (ARDS) caused by COVID-19 and the evolving outcomes associated with its use throughout the pandemic's first two years [3]. Despite the life-saving potential of ECMO, it is associated with significant complications [4]. Hemolysis, the rupture

of red blood cells, may occur due to mechanical stress within the circuit induced by the pump or contact with fibers, leading to the release of free hemoglobin into the bloodstream [5–7]. While hemolysis in an ECMO circuit is more associated with the blood pump and cannulae, considering the oxygenator's shear stresses, which comprise the largest volume and area of the ECMO circuit, is essential. Pan et al. demonstrated the gradual hemolysis in a microfluidic device with arrays of narrow gaps representing the blood path in ECMO. Their study revealed that due to the squeeze of RBCs between the fibers, they deform periodically, resulting in the fatigue of RBCs, progressive changes in morphology, and the gradual loss of deformability, indicating the importance of considering the hemolysis of the oxygenator [8]. Blood clot formation, or thrombosis, is another critical issue, potentially resulting in ischemic events and compromising the effectiveness of the oxygenator [9–11].

^a Institute of Engineering Design and Product Development, TU Wien, Austria

^b Institute of Chemical, Environmental and Bioscience Engineering, TU Wien, Austria

^{*} Corresponding author. Institute of Engineering Design and Product Development, TU Wien, Austria. *E-mail address*: seyyed.monsefi@tuwien.ac.at (S.H. Monsefi Estakhrposhti).

These complications contribute to high mortality rates among ECMO patients [12–14]. Studies indicate that survival rates differ based on the specific type of ECMO used; for instance, veno-arterial (VA) ECMO has reported survival rates of approximately 40–60 %, while veno-venous (VV) ECMO showed survival rates around 21–37 % [15]. To address these challenges, optimizing the design of hollow fiber membrane oxygenators to enhance mass transfer efficiency and reduce the risk of hemolysis and thrombosis is essential.

Computational modeling is an effective method for simulating and analyzing the blood flow and gas transfer within the oxygenator. Many studies have utilized computational fluid dynamics (CFD) to investigate the effect of different fiber arrangements and other parameters on flow patterns and gas transfer rates. Taskin et al. developed a multi-fiber CFD model evaluating two different void fractions or fiber spacings. Their findings indicated that at lower flow rates, the mass transfer rates for the arrangement with a denser configuration were only slightly higher than those of the wider-spaced arrangement. However, at higher flow rates, the denser configuration appeared more favorable [16]. Kaesler et al. examined oxygen transfer efficiency in staggered, in-line, and three random configurations. Their study demonstrated that a random configuration chain of fibers forms areas of low blood velocity and affects oxygen transfer [17]. Santos et al. tested flow-aligned spacers for different cases and showed how the local Sherwood number varied in each scenario [18]. Lukitsch et al. developed a 3D CFD model of an oxygenator with a parallel flow configuration. Their study confirmed that increasing the blood flow rate increases the radial velocity and improves specific CO₂ removal [19].

Additionally, research findings have demonstrated that changing the shape and arrangement of fibers may significantly influence gas exchange efficiency. Ecker et al. demonstrated that sinusoidal-shaped hollow fibers increase the available gas exchange surface, thereby improving CO₂ transfer rates. Their findings also indicated that gas transfer efficiency is higher when fibers are arranged in a staggered configuration compared to a non-staggered arrangement [20]. Furthermore, advancements in membrane materials, such as polymethylpentene (PMP) fibers, have enhanced biocompatibility and reduced thrombogenicity. PMP fibers improve gas permeability and lower resistance to blood flow, which helps reduce the risk of hemolysis and thrombosis [21]. These ongoing studies aim to advance ECMO technology by integrating computational modeling with experimental validation to develop oxygenators that optimize gas exchange and reduce complications, thereby improving patient outcomes.

Even though previous studies have utilized CFD to simulate gas transfer in hollow fiber membrane oxygenators with various fiber configurations, they have mainly focused on the fiber scale to evaluate mass transfer and neglected the critical complications of hemolysis and thrombosis. On the other hand, some studies have investigated blood damage, such as thrombosis in oxygenators, in a macroscopic way. These studies modeled a hollow fiber membrane as a porous medium. For instance, Fu et al. conducted CFD simulations to investigate the thrombosis risk in four clinical and one newly designed oxygenator [22]. CFD models that use a porous media approach are commonly employed to simulate the behavior of entire ECMO oxygenators. Since there are more than 10000 fibers in oxygenators, it is very hard to simulate the full oxygenator with all the fibers. In many studies, fibers were treated as a porous medium to neglect the complex geometry of the fiber bundle, allowing macroscopic flow and mass transfer evaluation [22-26]. However, at the fiber-scale level, only a very limited section of the oxygenator can be effectively investigated due to the computational cost. While these models simulate the thrombosis in the oxygenator, they do not include detailed blood damage modeling between the fibers. The micro-CT images from Wagner's study show many clot formations between the fibers, representing the importance of microscopically investigating the blood damage [27]. Optimizing fiber arrangements without addressing these risks limits progress in oxygenator design. Therefore, an optimization approach is required to evaluate gas exchange efficiency while minimizing the risks of hemolysis and thrombosis.

The primary aim of this study is to identify and analyze the interrelations between key geometric parameters of ECMO oxygenators, including fiber spacing, diameter, and bundle arrangement, and their effects on gas exchange efficiency, hemolysis, and thrombosis. By developing multivariate models to predict these outcomes, the study enhances understanding of how design choices influence oxygenator performance and blood damage. Following this, optimization methods, including Pareto front analysis, are applied to identify optimal configurations that maximize gas transfer efficiency while minimizing blood damage.

2. Materials and methods

2.1. Computational fluid dynamics

2.1.1. Geometric parameters

Three geometric parameters, including angle, diameter, and distance-to-diameter ratio, as well as a flow parameter, blood flow rate, were considered to optimize the membrane fiber arrangement. Fig. 1(a) shows the angle, diameter, and distance between the fibers in a staggered arrangement. Each parameter was assigned a specific lower and upper bound: the angle ranged from 30 to 60°, the diameter ranged from 300 to 700 μ m, the distance-to-diameter ratio ranged from 1.25 to 2.25, and the blood flow rate ranged from 0.5 to 5 L.min⁻¹. Blood flow rate was incorporated as an input parameter because flow condition variation might significantly influence the behavior of the geometric configuration of the fibers, thereby impacting the overall performance. Since the distance between the fibers may be impractical in some cases, the distance-to-diameter ratio was considered. For instance, in fibers with a diameter of 300 μ m, a distance of 500 μ m (distance-to-diameter ratio of 1.66) is feasible. In comparison, the exact distance is impossible in fibers with a diameter of 600 μm (distance-to-diameter ratio of 0.83) as the fibers collide.

2.1.2. Numerical domain

The computational fluid dynamics (CFD) domain was designed with 27 fibers, including 22 full fibers within the flow path and 10 half fibers at the periodic boundaries. Since simulations with more fibers produce results similar to the 27-fiber configuration, the CFD model with the 27-fiber configuration was chosen to better balance computational cost and accuracy. Given the laminar flow and unidirectional fiber alignment, a 2D flow assumption was considered appropriate for the CFD model, reducing the computational cost compared to a 3D model while maintaining accuracy. Inlet and outlet extensions of 6 mm each was added to the domain to achieve fully developed flow conditions. Fig. 1(b) shows the CFD domain along with dimensions, considering the arrangement with a 45 $^{\circ}$ fiber angle, a fiber diameter of 400 μ m, and a spacing of 600 μ m between fibers, giving a distance-to-diameter ratio of 1.5.

2.1.3. Governing equations, boundary conditions, and simulation settings The steady-state flow of blood is modeled by solving incompressible Navier-Stokes equations,

$$\rho\left(\frac{\partial \mathbf{v}}{\partial t} + (\mathbf{v} \cdot \nabla)\mathbf{v}\right) = -\nabla p + \mu \nabla^2 \mathbf{v}$$
(1)

$$\nabla . \mathbf{v} = 0, \tag{2}$$

where ρ is the fluid density in kg m⁻³, ${\bf v}$ is the fluid velocity vector in m s⁻¹, p is the pressure in Pa, and μ is the fluid viscosity in Pa s. These equations express the momentum conservation in a differential control volume. Solving the Navier-Stokes equations with appropriate initial and boundary conditions yields the velocity and pressure distributions throughout each control volume in the discretized computational

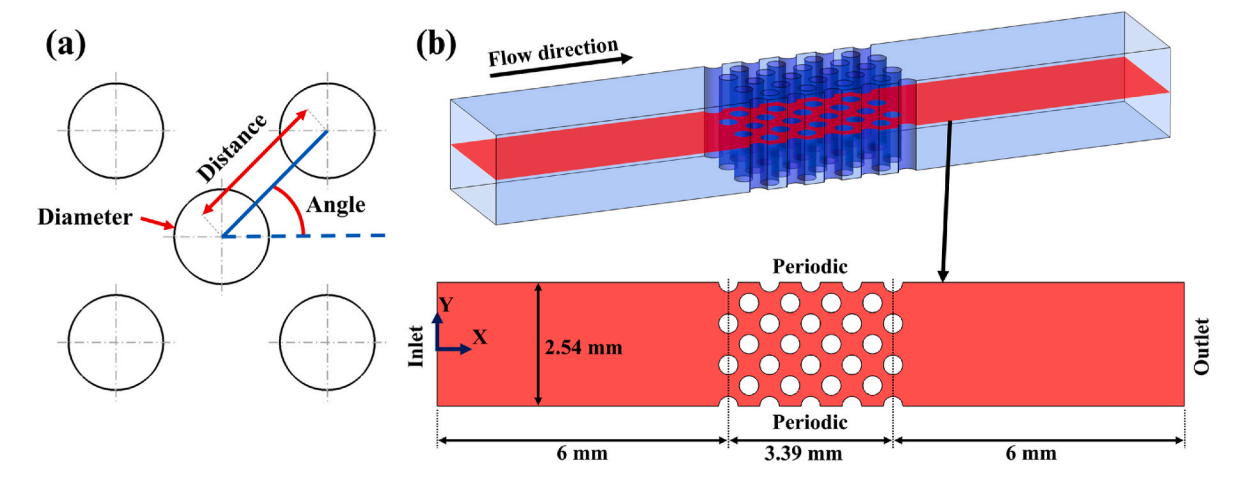


Fig. 1. Geometric and computational domain setup for fiber arrangement. (a) Defined geometric parameters for fibers in a staggered arrangement, (b) CFD domain layout with 27 fibers, showing flow direction, dimensions, and boundary conditions.

domain. Ansys Fluent (Ansys, Inc., Pennsylvania, USA) was used to solve the Navier-Stokes equations for the CFD simulations.

In this study, blood is treated as a non-Newtonian fluid, following a Carreau-Yasuda viscosity model, with a constant density of 1050 kg m $^{-3}$ [28]. The Reynolds number is calculated utilizing Equations (3) and (4), where Q represents the blood flow rate in m 3 s $^{-1}, L$ the distance between the fibers in m, θ the angle between the fibers in degrees, V the inlet blood velocity in m s $^{-1}$, D the fibers diameter in m, and μ_{∞} the infinite shear rate viscosity in Pa s. Considering an infinite shear rate viscosity of 0.0035 Pa s [28], a maximum flow rate of 5 L min $^{-1}$, a minimum distance-to-diameter ratio of 1.25 and a minimum angle of 30 $^{\circ}$, results in the maximum Reynolds number of 33.33, indicating laminar flow condition.

$$Q = A V = (6 \times L \times \sin(\theta) \times 1) \times V$$
(3)

$$Re = \frac{\rho VD}{\mu_{\infty}} = \frac{\rho Q}{6 \mu_{\infty} \frac{L}{D} \sin(\theta)}$$
 (4)

Fig. 1(b) shows the applied boundary conditions on the CFD domain. At the inlet, a constant velocity and at the outlet, a constant gauge pressure of 0 Pa was imposed. Periodic boundary condition was considered for the upper and lower sides of the domain, indicating a repetitive fiber arrangement and flow pattern. Period boundary conditions are suitable here, allowing the simulation to model only a section of fibers rather than the entire oxygenator. The Coupled scheme was used for pressure-velocity coupling, with pressure discretized using a second-order scheme and momentum using a second-order upwind scheme. A convergence value of 10^{-5} was set for all the variables.

2.1.4. Mass transport simulations

The steady-state transport of the gas is modeled by solving the advection-diffusion equation,

$$\nabla \varphi = D\nabla^2 \varphi + S,\tag{5}$$

where φ is the scalar quantity, D is the diffusion coefficient in m^2 s⁻¹, and S is the source term in s⁻¹. Since the CO_2 and O_2 exchange rates are in the same range [29–31] and given that CO_2 removal is generally the limiting factor in ECMO system performance, only CO_2 removal is considered in this study. This approach was chosen to reduce computational cost, simplify the optimization process, and avoid unnecessary complexity, as simulating both gases was deemed redundant due to their similar trends and transfer rate ranges.

A user-defined scalar (UDS) was used to solve the advection-diffusion equation. Based on the study by Svitek and Federspiel, the ${\rm CO_2}$ partial pressure is modeled by solving the following equation:

$$\nabla \cdot (\mathbf{v} \cdot P_{CO_2}) = \nabla \cdot (D_{eff,CO_2} \nabla P_{CO_2}), \tag{6}$$

where D_{eff,CO_2} is the effective diffusivity of CO₂, which is a combination of diffusion coefficient of CO₂, HCO $_3^-$, and bounded CO₂. The effective diffusivity of CO₂ is calculated as follows:

$$D_{eff,CO_2} = \frac{D_{CO_2} + \frac{D_{HCO_3}}{a_{CO_2}} \lambda_{CO_2}}{1 + \frac{1}{a_{CO_2}} \lambda_{CO_2}}$$
(7)

where D_{CO_2} is the diffusivity of dissolved CO_2 , D_{HCO_3} is the diffusivity of bicarbonate, α_{CO_2} is the CO_2 solubility, and α_{CO_2} is the slope of the CO_2 content curve [32]. A constant CO_2 partial pressure of 45 mmHg was set at the inlet, and a partial pressure of 4 mmHg was imposed on the fiber surfaces. At the outlet, a zero gradient CO_2 partial pressure was applied. The UDS was discretized using a second-order scheme, with a convergence criterion set to 10^{-5} . The mass-weighted average of CO_2 partial pressure is calculated at the outlet, and by calculating the CO_2 concentration from the partial pressure [33,34], the CO_2 removal is calculated as follows:

$$CTR = Q_{blood} \left(C_{CO_2,inlet} - C_{CO_2,outlet} \right) \tag{8}$$

Where CTR is the rate of transferred CO_2 in mL_{CO2} min^{-1} m^{-2} , Q_{blood} is the blood flow rate in mL_{blood} min^{-1} , and C_{CO_2} is the CO_2 concentration in mL_{CO2} mL_{blood}^{-1} .

2.1.5. Hemolysis index evaluation

A practical method for evaluating hemolysis is the hemolysis index (HI), which simplifies the relationship between shear stress, exposure time, and red blood cell damage. Hemolysis is typically assessed using empirical models that link mechanical stress and exposure duration. This approach, which has been validated in numerous studies [35,36], offers a direct and computationally efficient way to evaluate hemolysis. The hemolysis index was modeled by solving the advection equation,

$$\frac{d(HI')}{dt} + \rho(\mathbf{v}.\nabla HI') = S,$$
(9)

where H' is defined as a user-defined scalar variable equal to $H^{1/\alpha}$, and S is the source term given by $S = \rho (C \sigma^{\beta})^{1/\alpha}$. C, α , and β are the empirical coefficients equal to 3.62×10^{-5} , 0.785, and 2.416, respectively [35,36]. The scalar shear stress, σ , is calculated using Equation (10):

$$\sigma = \left[\frac{1}{6}\sum \left(\sigma_{ii} - \sigma_{jj}\right)^2 + \sum \sigma_{ij}^2\right]^{0.5} \tag{10}$$

where σ_{ij} are the shear stress components, and i and j are indices representing the coordinate directions in a Cartesian coordinate system.

2.1.6. Mesh dependence study

A mesh dependence study was done to ensure that the simulation results were independent of the mesh size and that the modeled physical phenomena were accurately captured. A structured mesh provides higher accuracy and lower computational cost than an unstructured mesh due to its regular and grid-like cell arrangement, reducing the numerical diffusion. Therefore, a structured mesh was generated for a smoother gradient, better convergence, and stability. The mesh was refined for the configuration with a 45 $^{\circ}$ fiber angle, a fiber diameter of 400 μm , a spacing of 600 μm between fibers, and a blood flow rate of 0.75 L min $^{-1}$. Four different meshes with the minimum orthogonal quality of 0.65 and a number of elements of 50k, 100k, 250k, and 500k were generated, and the local Sherwood number was evaluated for each. The local Sherwood number was calculated based on the following equation:

$$Sh = \frac{k_c L}{D_{CO_2}} \tag{11}$$

where L denotes the characteristic length in m, which in this context corresponds to the diameter of the fibers, D_{CO_2} represents the diffusion coefficient of the CO₂, and k_c is the local mass transfer coefficient in m s⁻¹ that was calculated based on the following equation:

$$k_c = -\frac{D_{CO_2}}{P_{CO_2,inlet}} \frac{\partial P_{CO_2}}{\partial n} \tag{12}$$

Root mean square error (RMSE) for the Sherwood number for each mesh was calculated relative to the finest mesh (500k). The RMSE percentage for 50k, 100k, and 250k elements meshes were 10.89 %, 4.52 %, and 1.33 %, respectively. Since the RMSE between the 250k and 500k

element meshes is around 1 %, the 250k element mesh settings were selected for the CFD simulations, ensuring consistent element count across varying geometries and mesh configurations. The local Sherwood number along a fiber circumference and a generated mesh close-up with 250k elements are shown in supplementary material S.1.

2.2. Experimental setup and procedure

2.2.1. Microchannel fabrication

Four rectangular microchannels containing fibers with different angles, diameters, and distance to diameter ratios were 3D-printed to investigate the transverse flow conditions in a membrane oxygenator. Microchannels were 3D-printed with a Digital Light Processing (DLP) printer (Max X27, Asiga, New South Wales, Australia) using Nano Clear resin (FunToDo, Kotka, Finland) with fibers in a staggered position. The fibers are 3D-printed as cylinders inside the microchannels with a height of 1 mm. On the side of the channels, semi-cylinders were 3D-printed, implying the periodic boundary condition. Fig. 2(a) shows the schematic of the microchannel with dimensions, and Fig. 2(b) shows the 3D-printed microchannel for the micro-particle image velocimetry (μ -PIV) experiment. The 4x magnification of the fibers under the microscope is shown in Fig. 2(c). Table 1 presents the geometric parameter values of the printed microchannels alongside the flow rate.

2.2.2. Micro-PIV measurement

For visualizing the flow and velocity field between the fibers of the fabricated micro-channel, a μ -PIV system was utilized. A simplified schematic of the μ -PIV system is shown in Fig. 2(d). Fluid flow (water) is seeded with polystyrene fluorescent micro-particles with a diameter of 1.9 μ m (PS-FluoRot-2.0, microParticles GmbH, Berlin, Germany). Since the density of the micro-particles (1.05 g cm⁻³) is similar to the density of the water (1 g cm⁻³), the micro-particles stay suspended in the water and move along the flow field. Fluid is pumped with the syringe pump

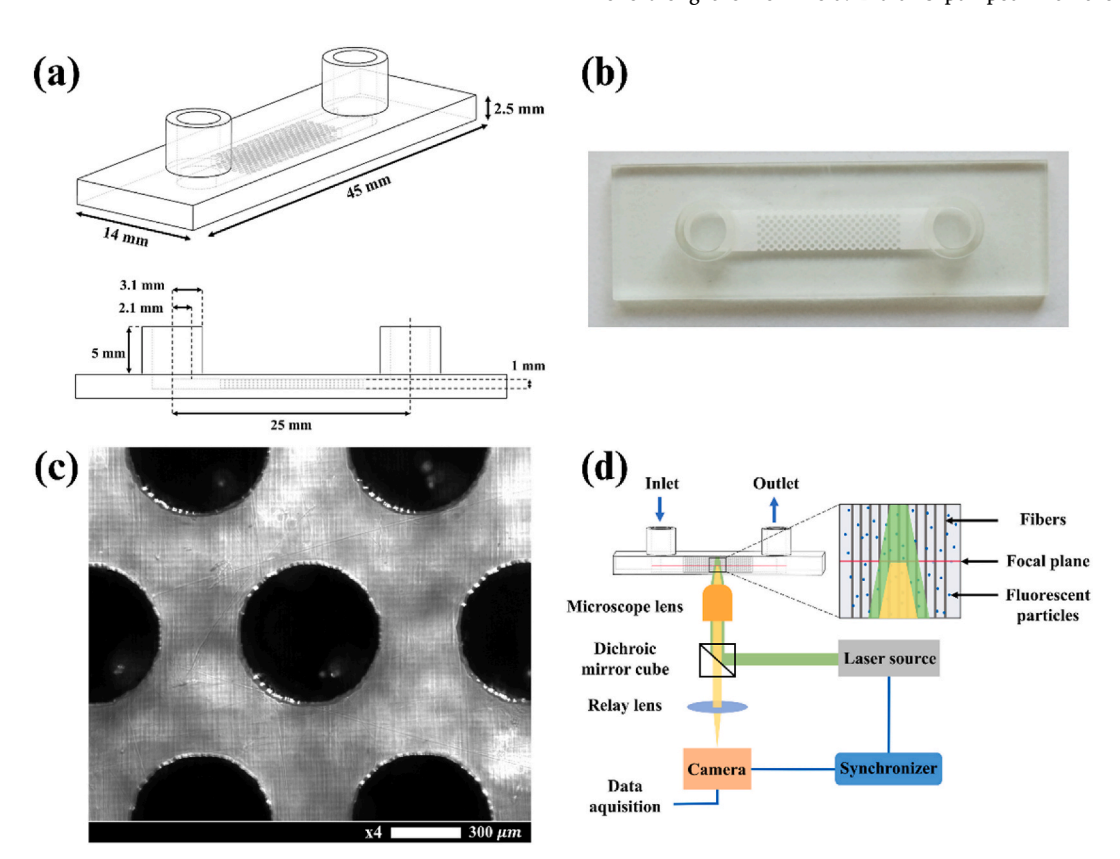


Fig. 2. Overview of microchannel design and measurement setup. (a) Detailed design of Microchannels, (b) 3D printed microchannel for the micro-PIV measurement, (c) Microchannel fibers under 4x magnification using the microscope, (d) Simplified schematic of the μ-PIV system.

Table 1Geometric parameter values of printed microchannels with the corresponding experiment flow rate.

Microchannel	Angle [°]	Diameter [μm]	Distance-to- Diameter Ratio [–	Flow Rate [mL min ⁻¹]
Case 1	60	600 (2 × 300)	900/600 = 1.5	1.5
Case 2	60	300	450/300 = 1.5	1. 5
Case 3	45	494 (1.3 × 380)	780/494 = 1.579	3
Case 4	45	380	600/380=1.579	3

(Model 11, Harvard Apparatus, Pennsylvania, USA) with a flow rate of 1.5 mL min⁻¹ and 3 mL min⁻¹. Two laser pulses are emitted from the laser source (Bernoulli B-PIV 200-15, Litron Lasers, Warwickshire, UK) with a time interval of 100 µs. Since the wavelength of the laser matches the absorption wavelength of the micro-particles, they excite at 530 nm and emit light at 607 nm, making them visible. The emitted light from the micro-particles inside the microchannel is captured by a high-speed CCD camera (Zyla 5.5 sCMOS, Andor Technology Ltd, Belfast, UK) that is mounted on an inverted microscope (IX73, Olympus Life Science, Tokyo, Japan), which provides magnified images of flow between the fibers. A synchronizer (LaserPulse Synchronizer 610036, TSI, Minnesota, USA) is used to precisely control the timing between the camera exposure and laser pulses, ensuring that two images are captured shortly after the laser pulses. The captured images are post-processed in the Insight 4G software (TSI, Minnesota, USA). Measurements were done at the midplane of the microchannel (shown as the focal plane). More details of the micro-PIV principle are given by Raffel et al. [37].

2.3. Data-driven model development

2.3.1. Multivariate polynomial model formulation

The primary objectives of ECMO are to enhance mass transfer while minimizing the risks of thrombosis and hemolysis. Therefore, three objectives were considered in this study:

- 1 Maximizing specific CO₂ removal: Specific CO₂ removal was calculated by dividing the CO₂ removal rate from Equation (8) by the total fiber surface area, indicating the mass transfer efficiency of the oxygenator.
- 2 Minimizing dead-zone-to-total-area ratio: Regions with a velocity below 0.1 mm s⁻¹ were defined as dead zones where blood flow is minimal and increases the risk of thrombosis. The dead-zone-to-total-area ratio measures the percentage of the oxygenator potentially susceptible to thrombosis.
- 3 Minimizing hemolysis index: Hemolysis index quantifies the extent of hemolysis, providing an estimate of blood cell damage.

In this study, blood-side pressure drop was not considered a direct optimization objective since the analysis focused on mass transfer efficiency, hemolysis, and thrombosis risk, which are more linked to patient safety and clinical outcomes. Besides, it was considered that the pump would manage any pressure loss, and its effects would be reflected indirectly through hemolysis, indicating hydraulic stress within the system. So, a higher pressure drop results in a higher mechanical load on the pump, which leads to higher shear-induced hemolysis.

The overview of the methodology employed in this study is shown in Fig. 4. After defining the input parameters and objectives, developing the CFD model, and conducting micro-PIV measurements for CFD validation, the fourth step involved generating 200 cases with varying input parameters using the Latin hypercube sampling (LHS) method [38]. CFD simulations were conducted for these cases to assess the effect of each defined parameter (angle, diameter, distance-to-diameter ratio, and blood flow rate) on the defined objectives. The dataset was divided into

a model identification dataset and a validation dataset to construct surrogate models for each objective. Specifically, 150 cases were used as model identification dataset to train the surrogate models, and the remaining 50 cases constituted the validation dataset where they were employed to assess the accuracy of the developed surrogate models.

As demonstrated in many studies, numerous physical phenomena exhibit nonlinear behavior. For instance, the Sherwood number in a laminar flow parallel to a plate is given as a function of the Reynolds number raised to the power of 1/2 and the Schmidt number raised to the power of 1/3 ($Sh=0.664\ Re^{1/2}\ SC^{1/3}$). However, by treating $Re^{1/2}$ and $Sc^{1/3}$ as separate variables, the Sherwood number equation can be expressed as a linear polynomial function of order 1 for each variable. So, an unknown exponent was assigned to each parameter to achieve a better fit to the data, and each objective is expressed as follows:

objective=
$$f$$
(angle^a,diameter^b,distance-to-diameterratio^c,flowrate^d)
(13)

where a, b, c, and d are the unknown exponents of each parameter, which vary for each objective. Additionally, the polynomial order is an unknown parameter that must be determined.

2.3.2. Modified Enhanced Jaya Algorithm

The Modified Enhanced Jaya algorithm, combining the modified Jaya algorithm for mixed variables [39] with the Enhanced Jaya Algorithm (EJAYA) [40], was implemented in MATLAB (MathWorks, Natick, Massachusetts, USA) and utilized to determine each objective's exponents and polynomial model. The unknown exponents were treated as continuous variables, constrained between -5 and 5, while the polynomial model was treated as a discrete variable, ranging from 1111 to 6666. Each digit in the polynomial model specifies the maximum degree of each input parameter in the multivariate polynomial model.

The Modified Enhanced Jaya algorithm was applied to minimize the fitness function for each objective. A multivariate polynomial model was fitted to the data for each population (parameters a, b, c, d, and the polynomial order). Using the input parameters from the model identification and validation datasets, the relative error of the obtained value from the multivariate polynomial model compared to the CFD was calculated as the fitness function. Additionally, 625 parameter combinations (5 values for each parameter) were generated and evaluated by the model. To enforce constraints, any negative output from the model resulted in a penalty value of 10^6 being assigned to the fitness function.

The EJAYA algorithm framework includes a search mechanism that consists of local exploitation and global exploration strategies. For each population, a switch probability is selected randomly. The global exploration strategy is applied if this value exceeds 0.5; otherwise, the local exploitation strategy is used. Since differential vectors between historical and current populations cover a broader search space than differential vectors within the same generation, the global exploration strategy can be particularly effective.

The discrete variable for polynomial order was treated as a continuous variable within the population generation. The generated value was then checked to find the two closest discrete values. If the generated value was greater than the average of these two values, it was assigned the higher value; otherwise, it was assigned the lower value.

3. Results

3.1. CFD validation with Micro-PIV

Different CFD simulations were conducted using a 3D domain, as shown in Fig. 1(b), to validate the results of the micro-PIV experiments. Unlike the main simulations, the validation simulations incorporated modified boundary conditions to align with the experimental setup; period boundary conditions were replaced with wall boundary conditions, and the working fluid was changed to water to replicate the actual

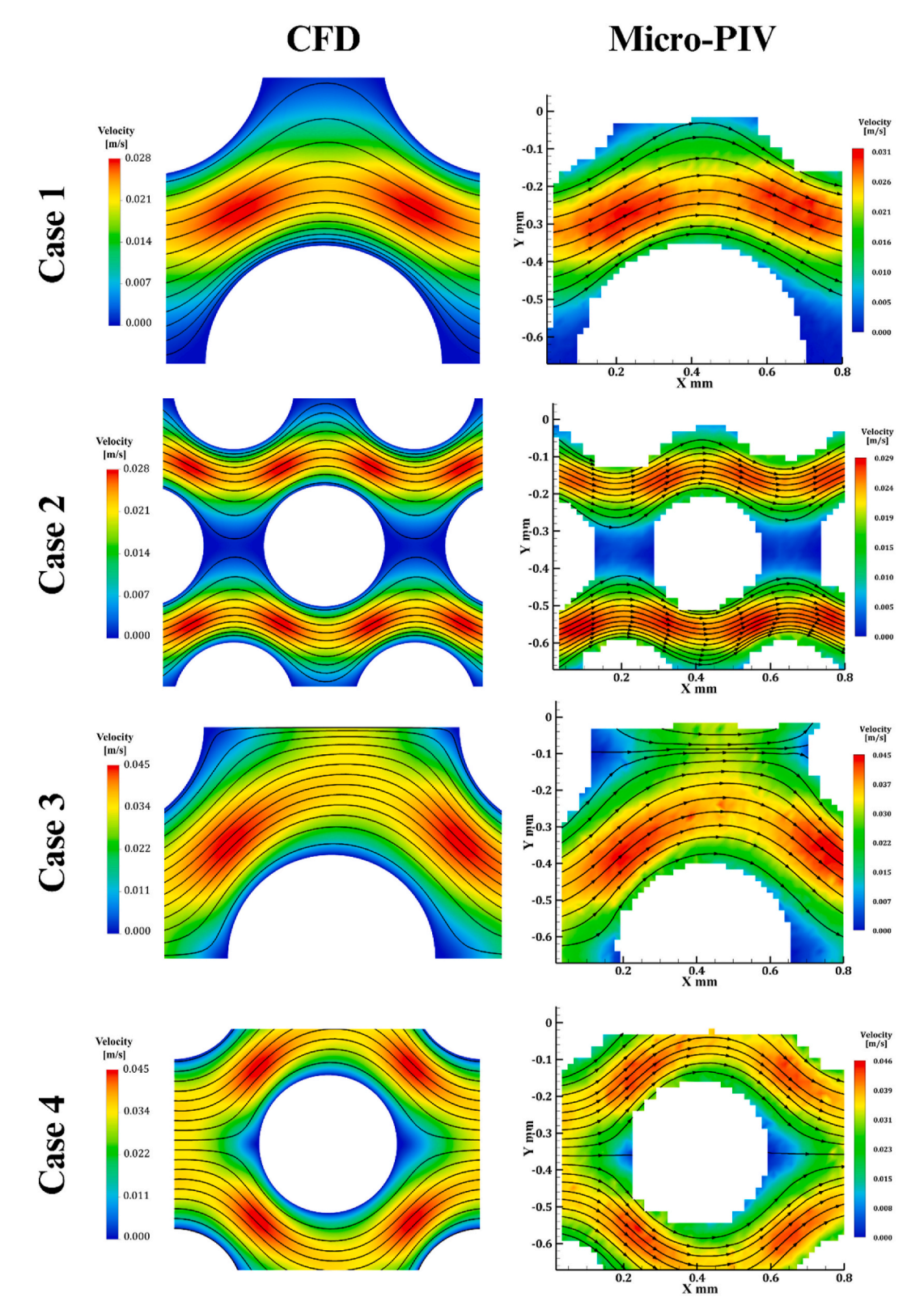


Fig. 3. Comparison of CFD simulations and micro-PIV experiments for four cases with different geometric parameters.

experimental conditions. Velocity contours were computed and visualized at the mid-plane of the domain for comparison. Fig. 3 compares the CFD simulation and the micro-PIV experiment results. Due to the inherent difficulty in defining a precise line in the micro-PIV experiment results to compare with the CFD results, a qualitative comparison approach was adopted. As shown in Fig. 3, the CFD simulations closely

align with the micro-PIV measurements, exhibiting strong agreement and confirming the robustness and accuracy of the CFD as an effective method to evaluate flow behavior between the fibers. With a 4x magnification, the field of view in the micro-PIV experiment was limited to 690^*820 microns. As a result, capturing the complete flow field around the entire fiber was impossible in cases 1 and 3.

Step 1: Define input parameters and objectives

Input parameters:

1- Angle
2- Diameter
3- Distance-to-diameter ratio
4- Blood flow rate

Objectives:
1- Specific CO₂ removal
2- Dead-zone-to-total-area ratio
3- Hemolysis index

Step 2: Create CFD model and mesh study

A CFD model was developed to evaluate the objectives, and a mesh independence study was conducted to determine the appropriate grid size for subsequent simulations.

Step 3: Micro-PIV measurement for CFD Valdation

Micro-PIV measurements were conducted for four cases to validate the velocity fields predicted by the CFD simulations.

Step 4: Create a dataset of 200 cases

The Latin Hypercube Sampling method generated 200 cases with varying input parameters. Of these, 150 cases were used as the model identification dataset to train the surrogate model, while the remaining 50 cases were used as a validation dataset to assess the model's accuracy.

Step 5: Use modified enhanced Jaya algorithm

The modified enhanced Jaya algorithm was employed to determine the unknown exponent of each input parameter and the polynomial order for each objective. The multivariate polynomial function representing each objective was formulated based on these values.

Step 6: Single-objective optimization

Single-objective optimization was performed using the surrogate models to determine each objective's minimum and maximum values.

Step 7: Multi-objective optimization

Multi-objective optimization was performed, and the Pareto front was obtained to identify the optimal configurations that balance all defined objectives. The weighted sum and goal programming methods were subsequently applied to select the most optimal fiber arrangement from the Pareto front solutions.

Fig. 4. Overview of the methodology employed in this study for the optimization of fiber arrangement in an oxygenator. The process includes parameter definition, CFD modeling, experimental validation, surrogate model development using a modified enhanced Jaya algorithm, and both single- and multi-objective optimization to identify optimal configurations.

3.2. Data distribution

Fig. 5 illustrates the relationship between the objectives (specific CO_2 removal, dead-zone-to-total-area ratio, and hemolysis index) and input parameters (angle, diameter, distance-to-diameter ratio, blood flow rate). The scatter plots indicate that most input parameters have a minimal correlation with the hemolysis index. However, there is a slight negative trend with the distance-to-diameter ratio, where a lower distance-to-diameter ratio tends to increase the hemolysis index, resulting in higher blood damage. Uniform scatter indicates a weak relationship with the hemolysis index between angle, diameter, and blood flow rate.

A more noticeable trend with angle and blood flow rate is shown with the dead-zone-to-total-area ratio. Lower angles and higher blood flow rates are associated with reducing the dead-zone area. A clear negative correlation exists between diameter and the specific CO_2 removal. Decreasing the diameter tends to increase the specific CO_2 removal. Also, a slight positive trend is observed between blood flow rate and specific CO_2 removal, with a higher flow rate increasing specific CO_2 removal.

As illustrated in Fig. 5, the majority of the data for the hemolysis index falls below 10×10^{-3} %, and most values for the dead-zone-to-total-area ratio are below 0.75 %. Additionally, specific CO₂ removal is mainly below 110 mL_{CO2} min⁻¹ m⁻².

3.3. Model evaluation of each objective

The modified enhanced Jaya algorithm has been employed to determine the unknown exponent for each input parameter and the polynomial order of the multivariate polynomial function. Stepwise regression was utilized to model the objectives. Stepwise regression removes predictors based on statistical criteria, such as p-values, allowing for selecting a subset of predictors that best aligns with the objectives. The calculated exponent values for each variable and the polynomial model for each objective are presented in Table 2. The final equation for each objective is provided in the supplementary material S.3.

Fig. 6 illustrates the accuracy of the obtained models for each mentioned objective. The obtained model for specific CO_2 removal, shows high accuracy for both the identification and validation datasets. The error between the predicted value and those obtained from the CFD simulations falls below 2.5 % for the model identification dataset. It remains below 5 % for the validation dataset except for one data point with an approximate error of 14 % (see Fig. 6(a)). The scatter plot of predicted versus actual specific CO_2 removal is shown in Fig. 6(b). The data points align closely with the identity line, indicating a strong agreement between the predicted and actual values for specific CO_2 removal. Low error percentages across both model identification and validation indicate that the model is highly accurate in predicting specific CO_2 removal.

The developed model predicting the dead-zone-to-total-area ratio demonstrates good accuracy as well. Fig. 6(c) illustrates the error percentage of this ratio as a function of input parameters. The error remains consistently below 15 %, indicating a good fit for the complex dataset. Even though most of the dead-zone-to-total-area ratio falls below 1, and only 7 data points show the dead-zone-to-total-area ratio above 1, the model shows a high accuracy across lower and higher values. Similarly, the close alignment of the predicted and actual values along the identity line implies that the model performs well (see Fig. 6(d)).

Fig. 6(e) presents the error percentage of the hemolysis index model. For this model, all the errors are below 5 %. Fig. 6(f) shows the predicted versus actual hemolysis index, where the data points align very closely to the identity line, meaning that the developed model performs well and provides high accuracy. Overall, all three models accurately fit the data, making them appropriate for further analysis.

3.4. Global Sensitivity Analysis

Uncertainty and sensitivity analysis are considered critical components in model applications. Global Sensitivity Analysis (GSA) helps to identify the key parameters whose uncertainty has the most significant impact on the output, allowing ranking of the variables, fixing or removing irrelevant ones, and reducing the complexity of the problem. Among the various GSA methods, variance-based Sobol' sensitivity indices are most commonly used due to their efficiency and ease of interpretation [41,42].

Several Sobol' indices exist, including the first-, second-, and higher-order indices. A second-order Sobol' indices can be defined as the first-order Sobol' index of a group of two input variables. In this study, the first- and total-order Sobol' indices were investigated. Azzini et al. proposed two sampling strategies along with their respective Monte Carlo estimators to calculate both the first- and total-order Sobol' indices [43]. Their findings demonstrate that the new strategy outperforms the previous one introduced by Saltelli [44]. Therefore, this study calculates the first-order and total Sobol indices following the methodology of Azzini et al. using the sample size of 10^7 .

The sensitivity analysis results, based on first-order and total-order Sobol' indices, are presented in Fig. 7. The distance-to-diameter ratio emerges as the most influential parameter across all objectives, both in terms of its direct effect and its interaction with other variables. This influence is particularly evident for the hemolysis index, where the Sobol' indices for the distance-to-diameter ratio show a notably higher contribution compared to the other inputs. In contrast, the blood flow rate demonstrates almost the least influence on all objectives.

The specific CO2 removal is most sensitive to the diameter and

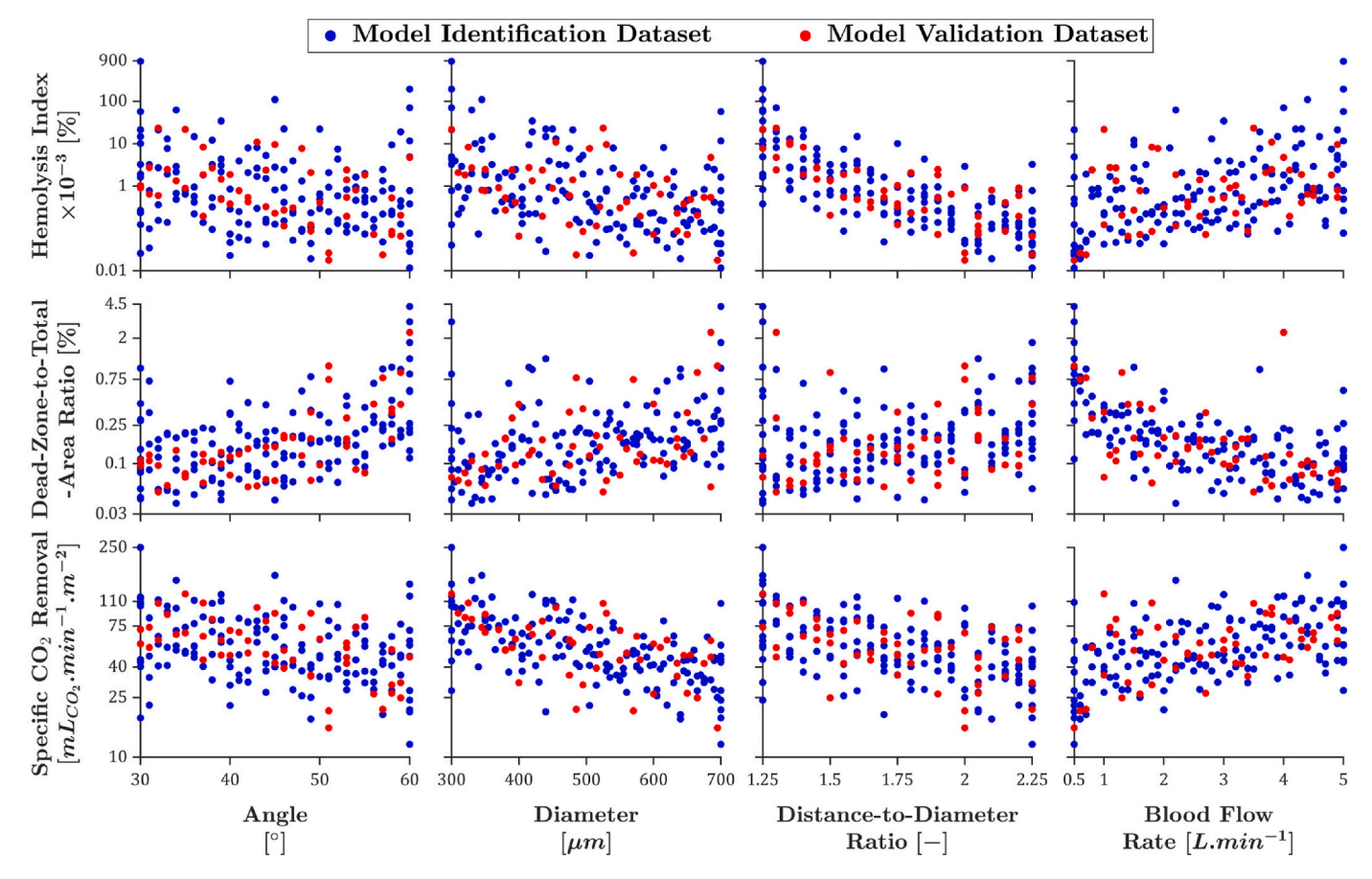


Fig. 5. Relationship between the objectives (specific CO₂ removal, dead-zone-to-total-area ratio, and hemolysis index) and input parameters (angle, diameter, distance-to-diameter ratio, blood flow rate) for the model identification (blue) and model validation (red) datasets.

Table 2Exponents and polynomial orders were achieved for each objective using the modified enhanced Jaya algorithm.

Objective	a	b	c	d	Polynomial Model
Specific CO ₂ Removal [mL _{CO₂} min ⁻¹ m ⁻²]	1.413	-0.251	-1.464	0.360	poly4666
Dead-Zone-to-Total- Area Ratio [%]	1.192	-0.093	-1.198	1.741	poly5546
Hemolysis Index $\times 10^{-3}$ [%]	0.597	-0.801	-2.691	-0.027	poly6452

distance-to-diameter ratio, while the dead-zone-to-total-area ratio is primarily influenced by the distance-to-diameter ratio and angle. However, for the dead-zone-to-total-area ratio, the variation in sensitivity indices between the inputs is less pronounced compared to the specific CO₂ removal and the hemolysis index. The total-order Sobol' indices, which account for the main effects and interactions among input variables, further support these findings.

3.5. Single-objective optimization

A single-objective optimization approach was conducted following the development of the multivariate polynomial models and the preliminary study of input parameter effects on each objective. A design space was constructed by defining each input parameter's minimum and maximum bounds. This space was discretized into a fine grid of data points, ensuring a thorough exploration of the objective landscape. Then, the objectives were evaluated at each of these discrete points using the developed polynomial models. Subsequently, the global

minimum and maximum values of each objective were identified. This method allows for a detailed understanding of the influence of the input parameters on the objectives and facilitates the identification of parameter configurations that yield the best possible outcomes for each objective. The minimum and maximum values of each objective are presented in Table 3. Since the aims are to maximize the specific $\rm CO_2$ removal and minimize the dead-zone-to-total-area ratio and the hemolysis index, the input parameter configurations that achieve these outcomes are highlighted in bold in Table 3.

3.6. Multi-objective optimization

In the multi-objective optimization analysis, the Pareto front was used to identify the optimal trade-offs between objectives. Despite the single-objective optimization that focuses on maximizing or minimizing a single objective, multi-objective optimization considers multiple objectives simultaneously. The aim is to identify solutions where improvements in one objective cannot be achieved without compromising another, known as non-dominated solutions. These solutions together form the Pareto front.

The Pareto front was constructed for all three objectives simultaneously. The resulting Pareto front provides a comprehensive view of the optimal solutions where no further improvement can be made in one objective without negatively impacting another. This approach enables the identification of balanced parameter configurations that consider all objectives, aiming to achieve the best fiber arrangement.

Fig. 8 shows the dominated and Pareto optimal solutions considering all three objectives. Pareto solutions are the non-dominated points, with no other points having higher specific CO_2 removal and lower dead-zone-to-total-area ratio and hemolysis index. The multi-objective

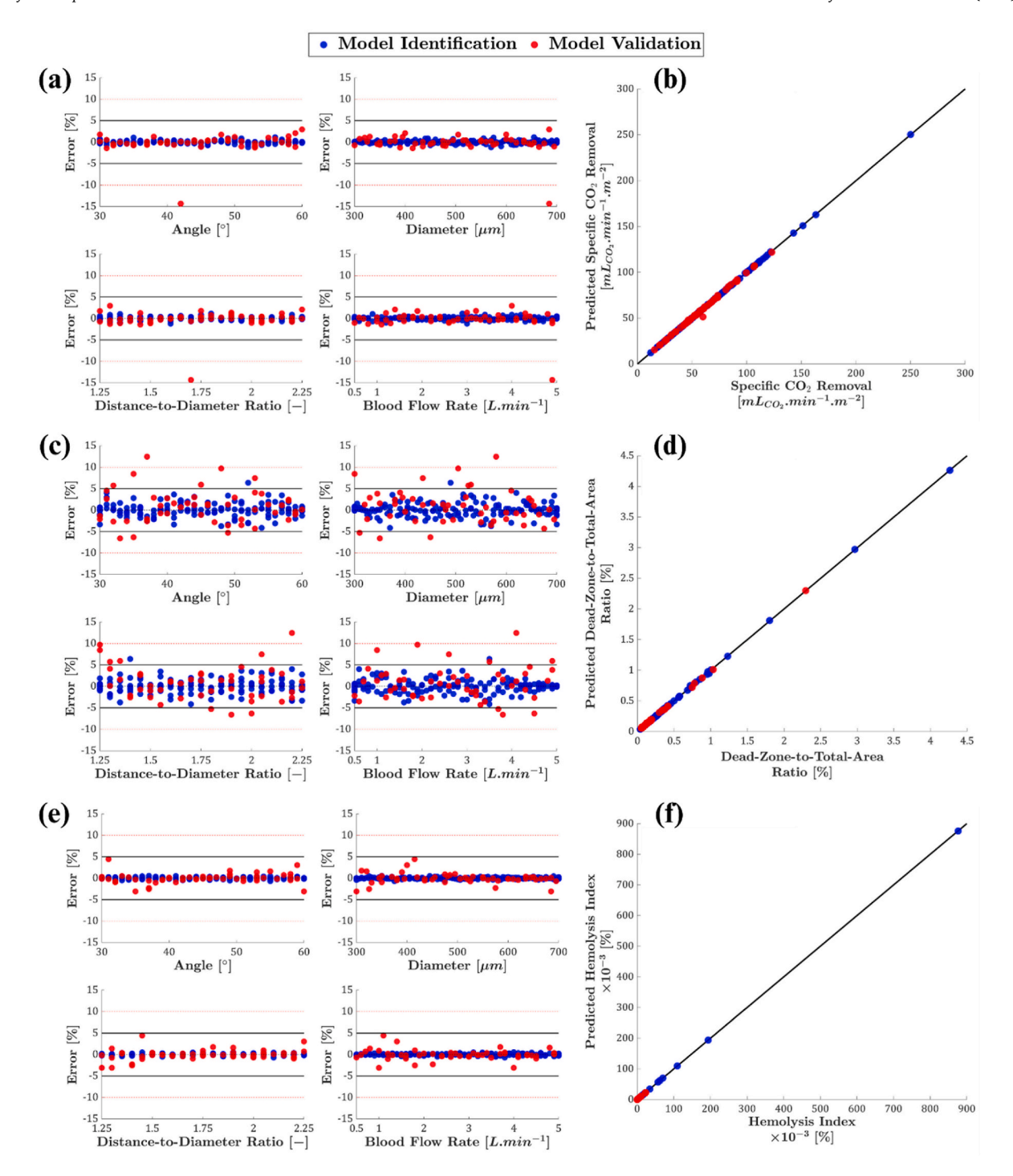


Fig. 6. Accuracy of the models for each objective: (a) Error percentage of specific CO₂ removal versus input parameters; (b) Predicted versus calculated value of the specific CO₂ removal from CFD; (c) Error percentage of dead-zone-to-total-area ratio versus input parameters; (d) Predicted versus real value of the dead-zone-to-total-area ratio from CFD; (e) Error percentage of hemolysis index versus input parameters; (f) Predicted versus real value of the hemolysis index from CFD.

Pareto front presents a comprehensive perspective on the trade-offs among specific CO_2 removal, dead-zone-to-total-area ratio, and hemolysis index. The multi-objective Pareto front indicates that enhancing specific CO_2 removal can significantly decrease the dead-zone-to-total-area ratio yet raises the hemolysis index, resulting in a precise balance in design choices.

Following obtaining the Pareto front solutions, two methods, weighted sum and goal programming, were employed to identify the optimal fiber arrangement.

3.6.1. Weighted sum method

The weighted sum method is a technique that combines several objectives into a single objective function by assigning a weight to each, allowing for prioritized trade-offs among the objectives [45]. In this study, the method balances the maximization of specific $\rm CO_2$ removal alongside the minimization of hemolysis index and dead-zone-to-total-area ratio by adjusting the relative importance of each objective.

The primary advantages of the weighted sum method are its simplicity and flexibility, as it allows objectives to be emphasized ac-

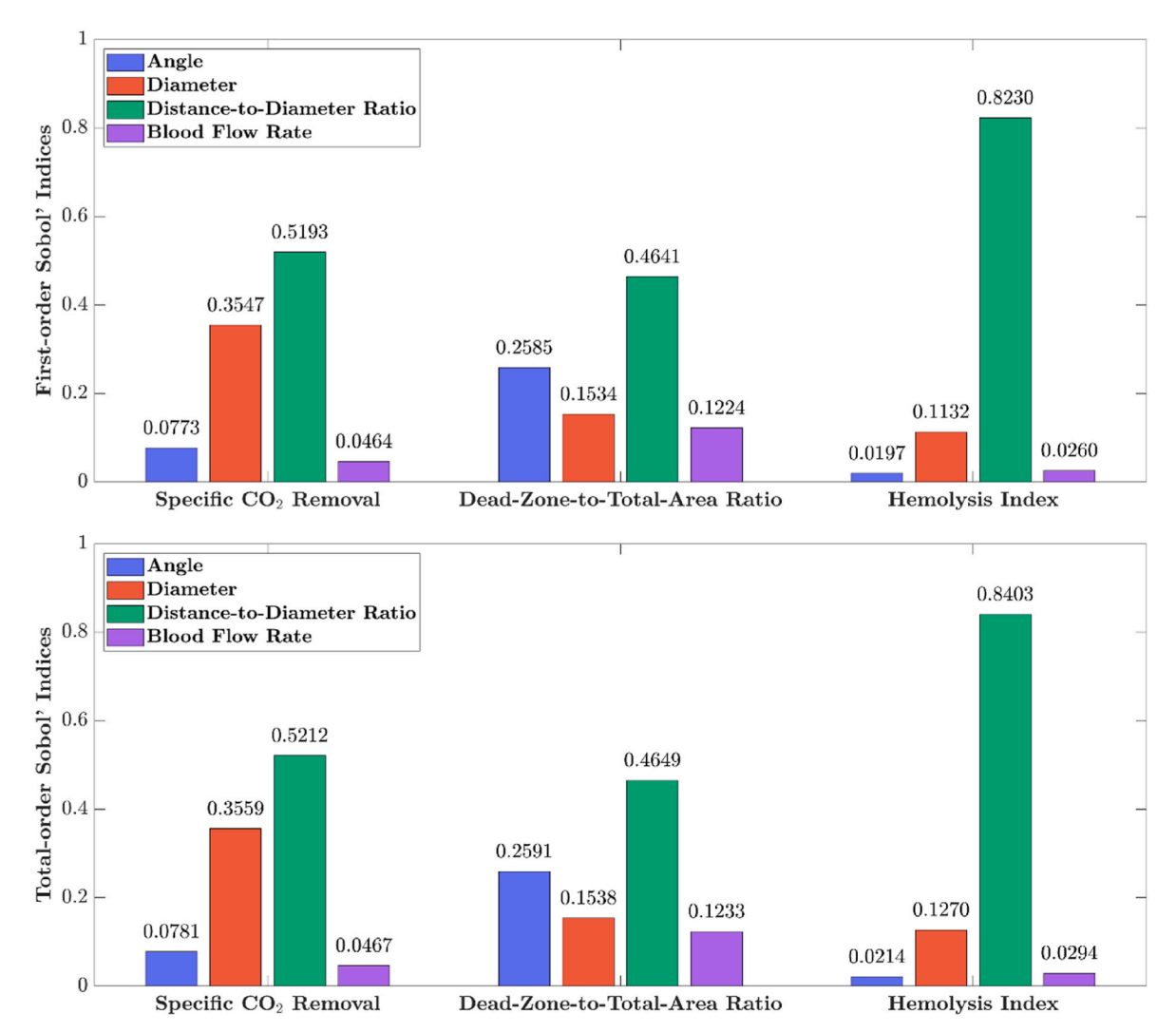


Fig. 7. Bar graph of first- and total-order Sobol' indices (respectively at the top and the bottom) with a sample size of 10⁷.

Table 3 Single-objective optimization results.

Objective	Min/Max	Angle [°]	Diameter [µm]	Distance-to-Diameter Ratio [-]	Flow Rate [L.min ⁻¹]
Specific CO ₂ Removal [mL _{CO₂} min ⁻¹ m ⁻²]	Min = 12.2	30	700	2.25	0.5
1	Max = 250.3	30	300	1.25	5
Dead-Zone-to-Total-Area Ratio [%]	Min = 0.024	34	300	1.55	4.8
	Max = 7.54	60	700	1.35	0.5
Hemolysis Index ×10 ⁻³ [%]	Min = 0.011	60	700	2.25	0.5
•	Max = 876	30	300	1.25	5

cording to specific needs by modifying the weights. However, this approach has limitations, including the subjectivity in weight selection, which may influence the outcome [46]. The best 3 optimal arrangements based on the weighted sum method for various weights are presented in Table 4. As shown in Table 4, the optimal arrangements achieved with the lowest diameter (300 μm), lower angles, and highest blood flow rate (5 L min $^{-1}$). Furthermore, assuming almost the same angle, by increasing the distance-to-diameter ratio from 1.25 to 1.65, the specific CO2 removal decreases from 220 to 130 mL_{CO2} min $^{-1}$ m $^{-2}$ (-41 %), while the hemolysis index decreases from 285× 10^{-3} to 12×10^{-3} % (-95.8%).

3.6.2. Goal programming method

The goal programming method is another technique that seeks to

achieve predefined target values or thresholds for each objective, minimizing the deviation from these set goals [47]. The primary advantages of goal programming lie in its ability to precisely align with clinical requirements by establishing explicit performance targets, reducing subjective prioritization often seen in other methods [48]. However, this approach also presents challenges, such as the difficulty in setting realistic and attainable target values and a potential risk of generating unbalanced or infeasible solutions if the set goals are overly restrictive or incompatible with each other. Considering the maximum value of the specific CO₂ removal (250.3 mL_{CO2} min⁻¹ m⁻²), the minimum value of hemolysis index (0.011 %), and the minimum value of dead-zone-to-total-area ratio (0.024 %) as the targets, the best 3 optimal arrangements using goal programming method are presented in Table 5.

The results of the goal programming method indicate that optimal

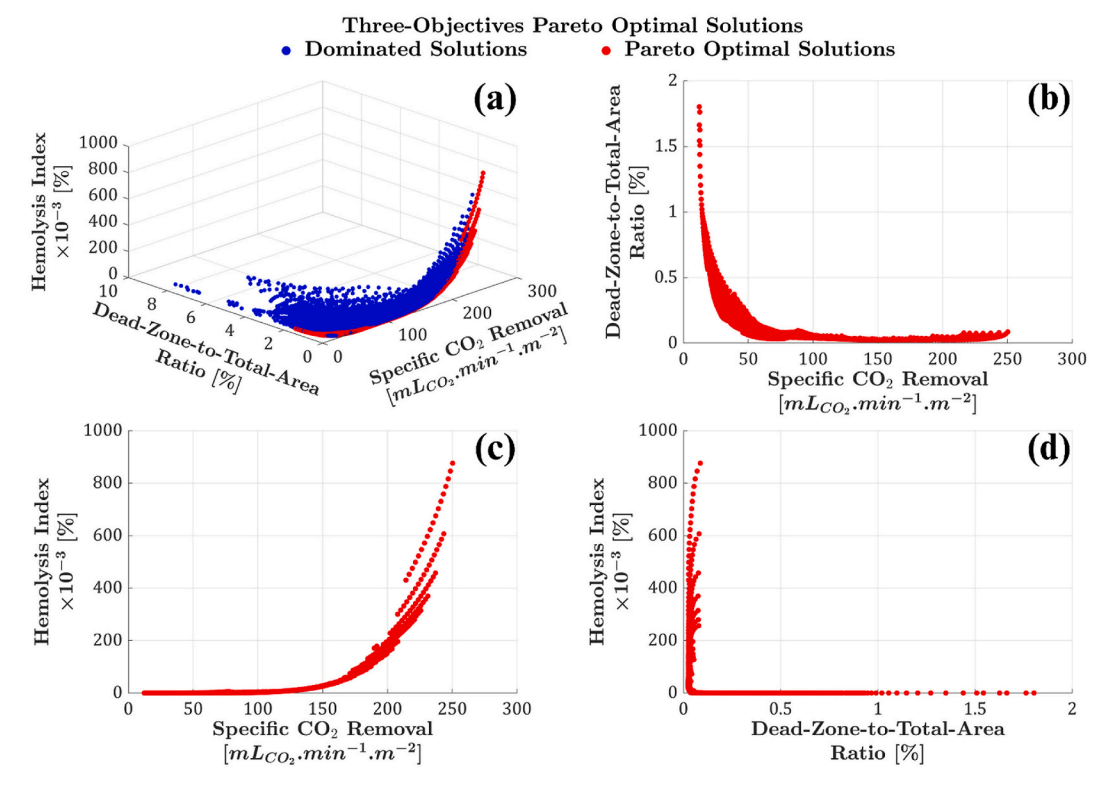


Fig. 8. Three-objective Pareto front solutions for the optimization of specific CO₂ removal, dead-zone-to-total-area ratio, and hemolysis index. (a) 3D representation of Pareto optimal solutions (red) and dominated solutions (blue). (b, c, d) Projection of three-objective Pareto front solutions onto each respective plane.

Table 4 The best three optimal fiber arrangements were determined using the weighted sum method for various weight combinations (w_1, w_2, w_3) .

Weights	Angle [[°]]	Diameter [μm]	Distance-to-Diameter Ratio [–]	Blood Flow Rate [L min ⁻¹]	Specific CO ₂ Removal [mL _{CO₂} min ⁻¹ m ⁻²]	Dead-Zone-to-Total- Area Ratio [%]	Hemolysis Index \times 10 ⁻³ [%]
$w_1 = 1/3$	30	300	1.25	5	250.3	0.086	876
$w_2 = 1/3$	30	300	1.25	4.9	248.6	0.070	846
$w_3 = 1/3$	30	300	1.25	4.8	246.9	0.060	816
$w_1 = 0.7$	31	300	1.25	5	243.4	0.080	607
$w_2 = 0.2$	32	300	1.25	5	237.1	0.076	457
$w_3 = 0.1$	31	300	1.25	4.9	241.7	0.064	586
$w_1 = 0.2$	34	300	1.25	4.7	220.3	0.045	284
$w_2 = 0.7$	34	300	1.25	4.8	222.1	0.050	294
$w_3 = 0.1$	34	300	1.25	4.6	218.4	0.041	274
$w_1 = 0.1$	37	300	1.65	5	130.8	0.031	11
$w_2 = 0.2$	36	300	1.65	5	132.5	0.029	12
$w_3 = 0.7$	38	300	1.6	5	134.6	0.031	13

solutions are achieved with the smallest fiber diameter and the highest blood flow rate. Moreover, the hemolysis index obtained using this method is lower than that achieved with the weighted sum method, particularly when higher weights are assigned to specific ${\rm CO_2}$ removal or the dead-zone-to-total-area ratio.

In both the weighted sum and goal programming methods, selecting different weights or setting alternative goals impacts the optimization

outcome, often resulting in different results. Therefore, assigning these values must carefully consider the relative importance of each objective within the context of critical care, as specific outcomes such as minimizing hemolysis or maximizing mass transfer may take superiority depending on clinical priorities and patient-specific requirements.

 Table 5

 The best three optimal arrangements were determined using the goal programming method, considering the best single objectives as targets.

Optimal Solutions	Angle [°]	Diameter $[\mu m]$	Distance-to-Diameter Ratio [–]	Blood Flow Rate [L min ⁻¹]	Specific CO ₂ Removal [mL _{CO2} min ⁻¹ m ⁻²]	Dead-Zone-to-Total- Area Ratio [%]	Hemolysis Index ×10 ⁻³ [%]
Optimal Solution 1	34	300	1.45	5	164.4	0.027	46
Optimal Solution 2	36	300	1.4	5	168.9	0.032	53
Optimal Solution 3	35	300	1.45	5	161.8	0.027	41

4. Discussion

The solutions obtained from multi-objective optimization differ in geometric configuration compared to those from single-objective optimization. For instance, when optimizing only for specific CO $_2$ removal, the resulting geometry is characterized by a 30° fiber angle, 300 μm diameter, and a distance-to-diameter ratio of 1.25. This configuration forms a very dense fiber bundle, which is efficient in gas transfer but induces high hemolysis and pressure drop. In contrast, when applying multi-objective optimization using the goal programming method, the optimal geometry shifts to a 34° angle, the same 300 μm diameter, but with a more moderate distance-to-diameter ratio of 1.45. This configuration achieves a specific CO $_2$ removal of 164.4 mLCO $_2$ min $^{-1}$ m $^{-2}$, approximately 34% lower than the single-objective optimum. However, the hemolysis index is reduced by 94.7%, demonstrating that a modest compromise in mass transfer efficiency by increasing the distance-to-diameter ratio can substantially improve blood damage.

The specific CO_2 removal calculated in this study aligns closely with the experimental results reported in Svitek's study [32]. Although the detailed specifications of their first prototype fiber bundle module are not fully disclosed, the fiber diameter of 300 μ m and the specific CO_2 removal values, ranging from 50 to 75 mL_{CO2} min⁻¹ m⁻² for a blood flow rate of 0.75–2.25 L min⁻¹, are consistent with the CFD results obtained in the present study. For example, with a diameter of 320 μ m, a distance-to-diameter of 2.1, an angle of 38°, and a flow rate of 2.3 L min⁻¹, the calculated specific CO_2 removal was 68.9 mL_{CO2} min⁻¹ m⁻². Similarly, with a diameter of 315 μ m, a distance-to-diameter of 1.95, an angle of 43°, and a flow rate of 1.3 L min⁻¹, the calculated specific CO_2 removal was 58.5 mL_{CO2} min⁻¹ m⁻².

Typical fiber mat configurations used in existing oxygenators were examined to establish the relevance of our findings to commercial oxygenator designs. For example, Membrana® PMP fiber mats feature a packing density of 44 fibers per inch and a fiber diameter of 380 μm , resulting in an approximate center-to-center spacing of 600 μm [49], which corresponds to a fiber angle of 51.7° and a distance-to-diameter ratio of 1.27. As shown in Table 4, this configuration closely aligns with the optimal geometries identified through our multi-objective optimization using the weighted sum method, thereby supporting the practical applicability of our modeling approach.

Although this study focuses on evaluating and optimizing membrane fiber arrangements, practical implementation may differ due to inherent challenges, such as slight variations in fiber positioning and movement of fibers as the fluid flows around them. Therefore, this study thoroughly analyzed and optimized the ideal geometric configuration. It is acknowledged that using a 2D simulation model represents a limitation of this work. In the simulations, fibers were assumed to be transverse to the flow, effectively modeling a cross-sectional slice of the oxygenator. While this approach offers valuable insight into local flow behavior and mass transfer between fibers, it does not fully capture the three-dimensional flow complexities present in real devices, such as those with 90° stacked or 24° wound configurations, as Focke et al. [50] reported. Nonetheless, the 2D configuration used here closely resembles the 90° stacked arrangement and provides a computationally efficient parametric analysis and optimization framework.

Moreover, this study demonstrated that increasing mass transfer

leads to increased blood damage, a factor often overlooked in previous studies. Even though there are some solutions to mitigate blood damage, such as adding heparin to the blood to reduce the risk of thrombosis [51], this study showed that optimizing the arrangement of the fibers can also effectively reduce the blood damage.

5. Conclusion

This study focused on optimizing the arrangement of ideal hollow fiber membrane oxygenators to enhance specific CO_2 removal while reducing the hemolysis index and the dead-zone-to-total-area ratio. The study developed highly accurate tools for predicting gas exchange efficiency, hemolysis, and dead-zone formation across various fiber configurations by integrating CFD simulations with multivariate polynomial models. These models evaluated the effects of geometric parameters, including fiber angle, diameter, and distance-to-diameter ratio, and the flow parameter, blood flow rate, on each objective. The main findings of the study are outlined below:

- CFD simulations demonstrated a good agreement with micro-PIV measurements, validating the accuracy of the numerical model.
- Combining the modified enhanced Jaya algorithm and multivariate polynomial functions resulted in high-accuracy modeling of the objectives.
- The distance-to-diameter ratio had the most significant impact on the hemolysis index.
- Specific CO₂ removal was most sensitive to the fiber diameter and distance-to-diameter ratio.
- The dead-zone-to-total-area ratio was mainly influenced by the distance-to-diameter ratio and fiber angle.
- The optimal configuration is sensitive to the chosen weights (in the weighted sum method) or goal targets (in the goal programming method).
- \bullet Commercial fiber mat, Membrana® PMP (44 fibers/inch, 380 μ m diameter), were analyzed to assess how typical design parameters align with the optimized geometries identified in this study.

Overall, this study demonstrates that careful optimization of fiber arrangement parameters can balance high mass transfer efficiency and reduce the risk of hemolysis and thrombosis. The study provides a foundation for further refining ECMO designs, emphasizing the need for parameter-specific adjustments based on clinical priorities.

CRediT authorship contribution statement

Seyyed Hossein Monsefi Estakhrposhti: Writing – review & editing, Writing – original draft, Visualization, Software, Methodology, Investigation, Formal analysis, Data curation, Conceptualization. Jing Jing Xu: Validation. Margit Gföhler: Writing – review & editing, Supervision. Michael Harasek: Writing – review & editing, Supervision.

Declaration of competing interest

The authors would like to declare that there is no conflict of interest with this research.

Acknowledgements

This project has received funding from the European Union's Horizon Europe research and innovation programme under grant agreement N° 101130006.

The authors acknowledge TU Wien Bibliothek for financial support through its Open Access Funding Programme.

Appendix A. Supplementary data

Supplementary data to this article can be found online at https://doi.org/10.1016/j.memsci.2025.124228.

Data availability

Data will be made available on request.

References

- [1] M. Makhoul, K. Bitton-Worms, Z. Adler, A. Saeed, O. Cohen, G. Bolotin, Extracorporeal membrane oxygenation (ECMO)—A lifesaving technology. Review and single-center experience, Rambam Maimonides Med. J. 10 (2) (2019).
- [2] P. Betit, Technical advances in the field of ECMO, Respir. Care 63 (9) (September 2018) 1162–1173.
- [3] R.R. Ling, K. Ramanathan, J.J.L. Sim, S.N. Wong, Y. Chen, F. Amin, S.M. Fernando, B. Rochwerg, E. Fan, R.P. Barbaro, Evolving outcomes of extracorporeal membrane oxygenation during the first 2 years of the COVID-19 pandemic: a systematic review and meta-analysis, Crit. Care 26 (1) (2022) 147.
- [4] D.A. Murphy, L.E. Hockings, R.K. Andrews, C. Aubron, E.E. Gardiner, V. A. Pellegrino, A.K. Davis, Extracorporeal membrane oxygenation-hemostatic complications, Transfus. Med. Rev. 29 (2) (2015) 90–101.
- [5] H. Appelt, A. Philipp, T. Mueller, M. Foltan, M. Lubnow, D. Lunz, F. Zeman, K. Lehle, Factors associated with hemolysis during extracorporeal membrane oxygenation (ECMO)—Comparison of VA-versus VV ECMO, PLoS One 15 (1) (January 2020) e0227793.
- [6] C.H.H. Chan, K.K. Ki, M. Zhang, C. Asnicar, H.J. Cho, C. Ainola, M. Bouquet, S. Heinsar, J.P. Pauls, G. Li Bassi, e. al, Extracorporeal membrane oxygenationinduced hemolysis: an in vitro study to appraise causative factors, Membranes 11 (5) (2021) 313.
- [7] L.A. Materne, O. Hunsicker, M. Menk, J.A. Graw, Hemolysis in patients with extracorporeal membrane oxygenation therapy for severe acute respiratory distress Syndrome—A systematic review of the literature, Int. J. Med. Sci. 18 (8) (2021) 1730
- [8] Y. Pan, Y. Li, Y. Li, J. Li, H. Chen, Fatigue of red blood cells under periodic squeezes in ECMO, Proc. Natl. Acad. Sci. 119 (49) (2022) e2210819119.
- [9] S. Zeibi Shirejini, J. Carberry, Z.K. McQuilten, A.J. Burrell, S.D. Gregory, C. E. Hagemeyer, Current and future strategies to monitor and manage coagulation in ECMO patients, Thromb. J. 21 (1) (January 2023) 11.
- [10] J. Schaadt, Oxygenator thrombosis: an international phenomenon, Perfusion 14 (6) (1999) 425–435.
- [11] S.R. Olson, C.R. Murphree, D. Zonies, A.D. Meyer, O.J. McCarty, T.G. Deloughery, J.J. Shatzel, Thrombosis and bleeding in extracorporeal membrane oxygenation (ECMO) without anticoagulation: a systematic review, ASAIO J. 67 (3) (2021) 290–296.
- [12] W. Tang, W.-T. Zhang, J. Zhang, K.-H. Jiang, Y.-W. Ge, A.-B. Zheng, Q.-W. Wang, P. Xue, H.-L. Chen, Prevalence of hematologic complications on extracorporeal membranous oxygenation in critically ill pediatric patients: a systematic review and meta-analysis, Thromb. Res. 222 (February 2023) 75–84.
- [13] B. Treml, R. Breitkopf, Z. Bukumirić, M. Bachler, J. Boesch, S. Rajsic, ECMO predictors of mortality: a 10-year referral centre experience, J. Clin. Med. 11 (5) (2022) 1224.
- [14] B. Friedrichson, H. Mutlak, K. Zacharowski, F. Piekarski, Insight into ECMO, mortality and ARDS: a nationwide analysis of 45,647 ECMO runs, Crit. Care 25 (2021) 1–10.
- [15] M. Ostermann, N. Lumlertgul, Acute kidney injury in ECMO patients, in: Annual Update in Intensive Care and Emergency Medicine 2021, Springer, berlin, 2021, pp. 207–222
- [16] M.E. Taskin, K.H. Fraser, T. Zhang, B.P. Griffith, Z.J. Wu, Micro-scale modeling of flow and oxygen transfer in hollow-fiber membrane bundle, J. Membr. Sci. 362 (1–2) (October 2010) 172–183.
- [17] A. Kaesler, M. Rosen, P.C. Schlanstein, G. Wagner, S. Groß-Hardt, T. Schmitz-Rode, U. Steinseifer, J. Arens, How computational modeling can help to predict gas transfer in artificial lungs early in the design process, ASAIO J. 66 (6) (June 2020) 683–690.
- [18] J. Santos, V. Geraldes, S. Velizarov, J.G. Crespo, Investigation of flow patterns and mass transfer in membrane module channels filled with flow-aligned spacers using computational fluid dynamics (CFD), J. Membr. Sci. 305 (1–2) (November 2007) 103–117.

- [19] B. Lukitsch, P. Ecker, M. Elenkov, C. Janeczek, B. Haddadi, C. Jordan, C. Krenn, R. Ullrich, M. Gfoehler, M. Harasek, Computation of global and local mass transfer in hollow fiber membrane modules, Sustainability 12 (6) (March 2020) 2207.
- [20] P. Ecker, M. Pekovits, T. Yorov, B. Haddadi, B. Lukitsch, M. Elenkov, C. Janeczek, C. Jordan, M. Gfoehler, M. Harasek, Microstructured hollow fiber membranes: potential fiber shapes for extracorporeal membrane oxygenators, Membranes 11 (5) (May 2021) 374.
- [21] T. He, J. He, Z. Wang, Z. Cui, Modification strategies to improve the membrane hemocompatibility in extracorporeal membrane oxygenator (ECMO), Adv. Compos. Hybrid Mater. 4 (4) (December 2021) 847–864.
- [22] X. Fu, Z. Su, Y. Wang, A. Sun, L. Wang, X. Deng, Z. Chen, Y. Fan, Comparison of hemodynamic features and thrombosis risk of membrane oxygenators with different structures: a numerical study, Comput. Biol. Med. 159 (2023) 106907.
- [23] M. Gartner, C. Wilhelm, K. Gage, M. Fabrizio, W. Wagner, Modeling flow effects on thrombotic deposition in a membrane oxygenator, Artif. Organs 24 (1) (2000) 29–36
- [24] J. Zhang, T.D. Nolan, T. Zhang, B.P. Griffith, Z.J. Wu, Characterization of membrane blood oxygenation devices using computational fluid dynamics, J. Membr. Sci. 288 (1–2) (2007) 268–279.
- [25] B. Fill, M. Gartner, G. Johnson, M. Horner, J. Ma, Computational fluid flow and mass transfer of a functionally integrated pediatric pump-oxygenator configuration, ASAIO J. 54 (2) (2008) 214–219.
- [26] L. Goubergrits, B. Franke, Novel axial oxygenator with bevelled shape of priming volume: CFD based analysis of oxygenator hemodynamics, Curr. Direct. Biomed. Eng. 10 (4) (2024) 268–271.
- [27] M.S. Wagner, M. Kranz, L. Krenkel, D. Pointner, M. Foltan, M. Lubnow, K. Lehle, Computer based visualization of clot structures in extracorporeal membrane oxygenation and histological clot investigations for understanding thrombosis in membrane lungs, Front. Med. 11 (2024) 1416319.
- [28] S. Karimi, M. Dabagh, P. Vasava, M. Dadvar, B. Dabir, P. Jalali, Effect of rheological models on the hemodynamics within human aorta: CFD study on CT image-based geometry, J. Non-Newtonian Fluid Mech. 207 (2014) 42–52.
- [29] K.F. Bachmann, M. Haenggi, S.M. Jakob, J. Takala, L. Gattinoni, D. Berger, Gas exchange calculation May estimate changes in pulmonary blood flow during veno-arterial extracorporeal membrane oxygenation in a porcine model, Am. J. Physiol. Lung Cell. Mol. Physiol. 318 (6) (2020) L1211–L1221.
- [30] D.C. Berger, L. Zwicker, K. Nettelbeck, D. Casoni, P.P. Heinisch, H. Jenni, M. Haenggi, L. Gattinoni, K.F. Bachmann, Integral assessment of gas exchange during veno-arterial ECMO: accuracy and precision of a modified fick principle in a porcine model, Am. J. Physiol. Lung Cell. Mol. Physiol. 324 (2) (2023) L102–L113.
- [31] X. Li, X. Yu, A. Cheypesh, J. Li, Non-invasive measurements of energy expenditure and respiratory quotient by respiratory mass spectrometry in children on extracorporeal membrane Oxygenation-A pilot study, Artif. Organs 39 (9) (2015) 815–819.
- [32] R. Svitek, W. Federspiel, A mathematical model to predict $\rm CO_2$ removal in hollow fiber membrane oxygenators, Ann. Biomed. Eng. 36 (2008) 992–1003.
- [33] J. Loeppky, U. Luft, E. Fletcher, Quantitative description of whole blood CO2 dissociation curve and haldane effect, Respir. Physiol. 51 (2) (1983) 167–181.
- [34] L.B. Khadka, F.L. Mouzakis, A. Kashefi, J. Greven, K. Mottaghy, J.W. Spillner, Mathematical modeling of oxygen and carbon dioxide exchange in hollow fiber oxygenators, Membranes 14 (3) (2024) 68.
- [35] M. Taskin, K. Fraser, T. Zhang, C. Wu, B. Griffith, Z. Wu, Evaluation of Eulerian and Lagrangian models for hemolysis estimation, ASAIO J. 58 (4) (2012) 363–372.
- [36] K.H. Fraser, T. Zhang, M.E. Taskin, B.P. Griffith, Z.J. Wu, A quantitative comparison of mechanical blood damage parameters in rotary ventricular assist devices: shear stress, exposure time, and hemolysis index, J. Biomech. Eng. 134 (8) (2012).
- [37] M. Raffel, C.E. Willert, F. Scarano, C.J. Kähler, S.T. Wereley, J. Kompenhans, Particle Image Velocimetry: a Practical Guide, Springer, 2018.
- [38] R.L. Iman, Latin Hypercube Sampling, John Wiley & Sons, 2008.
- [39] P. Singh, H. Chaudhary, A modified jaya algorithm for mixed-variable optimization problems, J. Intell. Syst. 29 (1) (2019) 1007–1027.
- [40] Y. Zhang, A. Chi, S. Mirjalili, Enhanced jaya algorithm: a simple but efficient optimization method for constrained engineering design problems, Knowl. Base Syst. 233 (2021).
- [41] A. Saltelli, S. Tarantola, F. Campolongo, M. Ratto, Sensitivity Analysis in Practice: a Guide to Assessing Scientific Models, Wiley Online Library, 2004.
- [42] I.M. Sobol, Global sensitivity indices for nonlinear mathematical models and their monte carlo estimates, Math. Comput. Simulat. 55 (1–3) (2001) 271–280.
- [43] I. Azzini, T.A. Mara, R. Rosati, Comparison of two sets of monte carlo estimators of sobol' indices, Environ. Model. Software 144 (2021) 105167.
- [44] A. Saltelli, M. Ratto, S. Tarantola, F. Campolongo, Update 1 of: sensitivity analysis for chemical models, Chem. Rev. 112 (5) (2012) PR1–PR21.
- [45] R.T. Marler, J.S. Arora, The weighted sum method for multi-objective optimization: new insights, Struct. Multidiscip. Optim. 41 (2010) 853–862.
- [46] I.Y. Kim, O.L. de Weck, Adaptive weighted sum method for multiobjective optimization: a new method for pareto front generation, Struct. Multidiscip. Optim. 31 (2) (2006) 105–116.
- [47] A.H. Abdelhamid, R.H. Mohamed, M.M. Rashwan, A.R.A. Farag, Generating pareto optimal solutions for multi-objective optimization problems using goal programming, Contemp. Math. (2024) 3082–3097.
- [48] M. Tamiz, D. Jones, Goal programming and pareto efficiency, J. Inf. Optim. Sci. 17 (2) (1996) 291–307.

- [49] S.P. Madhani, B.D. D'Aloiso, B. Frankowski, W.J. Federspiel, Darcy permeability of hollow fiber membrane bundles made from membrana polymethylpentene fibers used in respiratory assist devices, ASAIO J. 62 (3) (2016) 329–331.
- [50] J.M. Focke, P.-L. Bonke, N. Gendron, T. Call, U. Steinseifer, J. Arens, M. Neidlin, The influence of membrane fiber arrangement on gas exchange in blood
- oxygenators: a combined numerical and experimental analysis, J. Membr. Sci. 710 (2024) 123147.
- [51] H.J. Yeo, D.H. Kim, D. Jeon, Y.S. Kim, W.H. Cho, Low-dose heparin during extracorporeal membrane oxygenation treatment in adults, Intensive Care Med. 41 (2015) 2020–2021.